Flow, Turbulence and Combustion (2025) 115:1729–1753
https://doi.org/10.1007/s10494-025-00691-2

RESEARCH

Influence of Obstacle Separation Distance on the Acceleration of Premixed Methane/Air Flames in a Closed Channel

Sebastian Valencia[1] · **Fernando Illacanchi**[1] · **Lucas de Azevedo**[2,3] · **Andres Z. Mendiburu**[2,3] · **Luis Bravo**[4] · **Prashant Khare**[5,6] · **Cesar Celis**[1]

Received: 23 December 2024 / Accepted: 18 August 2025 / Published online: 8 September 2025

Abstract

Flame acceleration plays an important role in determining the onset of deflagration-to-detonation transition (DDT) phenomenon that is relevant to novel pressure-gain propulsion and explosion safety research. Accordingly, this work explores the influence of the separation distance between obstacles (S) inside a 1050 mm closed duct on the acceleration of premixed flames fueled by a stoichiometric methane/air mixture at 40 kPa pressure. The studied duct geometry features a 96 mm x 96 mm square cross section and includes five obstacles along the wall with a 75% blockage ratio, each delineated by side dimensions of 96 mm x 96 mm and square holes of 48 mm x 48 mm. Experimental and direct numerical simulations (DNS) techniques are employed here to investigate the flame acceleration dynamics under different operating conditions. More specifically, high-speed video captures the dynamics of the flame front evolution from experiments, while DNS are carried out using the PeleC fully compressive Navier Stokes solver, including finite-rate chemistry and adaptive mesh refinement (AMR). A comparison between experimental and numerical results for $S = 1.0\ D_h$ shows reasonable agreement in flame tip velocity and reduced position, supporting the applicability of a two-dimensional DNS model like the one employed here. In contrast, for $S = 1.5\,D_h$ the numerical results fail to reproduce the experimentally observed flame structure and acceleration, likely due to missing three-dimensional effects. Numerical simulations for different S values ranging from 0.75 to 1.5 D_h reveal that obstacle spacing has a strong influence on flame acceleration mechanisms. As S increases indeed, the flame shifts from geometry-constrained jetting to instability-driven propagation involving vortex generation and pressure-wave interactions. The case with $S = 1.25\ D_h$ yields the highest flame tip velocity, even though the one with $S = 1.5\,D_h$ exhibits greater vorticity and pressure amplitudes. This is attributed to the reduced flame–vortex coupling coherence in the $S = 1.5\,D_h$ case, which results in more chaotic flame dynamics and lower flame acceleration efficiency. These results offer new insight into the mechanisms of flame acceleration under confinement and highlight obstacle spacing as a key design parameter for optimizing performance and safety in combustion systems.

Extended author information available on the last page of the article

Keywords Flame acceleration · Obstacle separation · Methane/air mixture · Experiments · Numerical modeling

1 Introduction

The intricate dynamics of flame acceleration and the deflagration-to-detonation transition (DDT) phenomena play a pivotal role in both the prevention of explosions in confined spaces and the development of novel engine concepts based on detonation-based propulsion (Xiao and Li 2023), especially within combustors of pulse detonation engines (PDE) and rotating detonation engines (RDE) (Xiao and Oran 2019). A fundamental understanding of flame acceleration is of paramount importance, since it establishes initial conditions for DDT. The rate of turbulence generation, crucial for rapid flames, is governed by the interactions of the flame with its surroundings, such as obstacles and other geometric configurations (Ciccarelli and Dorofeev 2008). Extensive research has focused on the interaction between flames and obstacles, revealing that the presence of obstructions frequently amplifies turbulent combustion. This leads in turn to a significant increase in both flame tip speed and explosion overpressure (Huang et al. 2021).

Numerous studies have been conducted to investigate how obstacles affect flame propagation and the dynamic characteristics of explosions. Obstacles enhance flame propagation by inducing and intensifying turbulence ahead of the premixed flame front of unburned combustible gas. The degree of turbulence is intricately linked to both the velocity of the flow field and the blockage ratio (Na'inna et al. 2013). When the flame progresses through turbulent flow, there is a marked increase in both the surface area, kinetic energy, and the heat release rate (Huang et al. 2021). The presence of obstacles has also been reported to induce bridging of the flame front wrinkling, leading to the transition from laminar to turbulent combustion (Zheng et al. 2023). In shock-flame interactions, a cascade of instabilities, including Rayleigh-Taylor (RT), Richmyer-Meshkov (RM) and the Kelvin-Helmholtz (KH) ones, are induced. These interactions, along with the flame-vortex interactions, significantly impact the onset and evolution of DDT (Huang et al. 2021).

Several previous studies have analyzed obstacle-related factors, including blockage ratio (BR), obstacle shape, and spacing. Increasing the number of obstacles has been shown to elevate explosion overpressure (Hall et al. 2009). The shape of obstacles significantly influences the evolution of the flame, it has been reported that obstacles with sharp edges and multiple corners exhibit faster acceleration (Park et al. 2007). The spacing and channel width have been observed to linearly increase the time and length of DDT, with higher obstacle density that accelerates the propagation of the flame (Gamezo et al. 2007). In a work examining different values of BR, it was found that when BR is relatively small, the unburned gas flow velocity is lower and the flame is easily entrained into the recirculation zone. However, in the presence of a larger BR, the shear layers are enhanced, leading to dominant propagation of the flame in the streamwise direction (Zheng et al. 2023). Kuznetsov et al. (Kuznetsov et al. 2002) identified critical diameters and lengths for specific blockage ratios in the DDT of methane-air mixtures, which impact flame velocity.

Direct numerical simulation (DNS) based techniques have also been extensively used in the past to explore the effects of obstacles on the propagation of deflagration flames (Zheng et al. 2023; Liu et al. 2023; Rudy and Teodorczyk 2020). Compared to experiments, DNS provide unprecedented insights into the underpinning mechanisms governing flame acceleration at spatio-temporal scales that remain out of reach of experimental techniques. Consequently, in this work, flame acceleration is investigated by presenting novel results with DNS and experimental techniques for both validation and exploration of the underpinning physics.

More specifically, this work investigates the influence on flame acceleration of five obstacles with a blockage ratio (BR) of 75% and different obstacle separation distances (S). Since many industrial explosion incidents involve primarily deflagrative propagation rather than detonative (Na'inna et al. 2014), the emphasis here is placed on deflagration. To capture the dynamics of the flame front, the methodology employed here involves conducting both physical and numerical experiments, using a high-speed video camera and solving the fully compressible two-dimensional Navier–Stokes equations along with finite rate kinetics. The numerical simulations involve the modeling of a closed channel containing a methane/air mixture and an array of square obstacles along the wall, placed to reproduce the experimental conditions. Subsequently, insights derived from these numerical simulations under different S values are discussed. With a focus on the interplay between the obstacles and the flame fronts, a description of the mechanisms (instabilities) driving flame acceleration is emphasized.

The novelty of this work lies in its systematic investigation of how obstacle separation distance influences the mechanisms governing flame acceleration in obstructed channels. Although the experimental and numerical methodologies employed are well-established, the contributions of this work relate to the comprehensive physical characterization of flame behavior across a range of obstacle spacings, identifying the transition between geometrically confined and instability-driven flame propagation regimes. By employing high-resolution DNS in a 2D domain indeed, this study captures the spatio-temporal evolution of key physical processes such as vortex–flame interaction, baroclinic torque generation, and pressure wave amplification, which are shown to strongly depend on obstacle spacing. The results obtained here provide new insight into how hydrodynamic instabilities and pressure–flame coupling contribute to flame acceleration in obstructed channels, offering practical implications for the design of combustion systems featuring deflagration-to-detonation transition (DDT) processes.

Summarizing what follows, Sect. 2 briefly describes the experimental setup employed to obtain the experimental results discussed here. In Sect. 3, the mathematical and numerical models used in this work are described. Finally, the main experimental and numerical results obtained here are discussed in Sect. 4, and some conclusions drawn from them are summarized in Sect. 5

2 Experimental Setup

The experimental facility employed in this work consisted of a mixing chamber, a propagation duct, a vacuum pump, obstacles inside the duct, a high-speed video camera, an ignition source, and a data acquisition system. The experimental setup is shown in Fig. 1. The experimental facility is located at the Universidad Federal Rio Grande do Sul in Brazil. In this work, only experiments involving stoichiometric natural gas (NG)/air mixtures were accounted for, even though the experimental setup also has hydrogen, nitrogen and helium

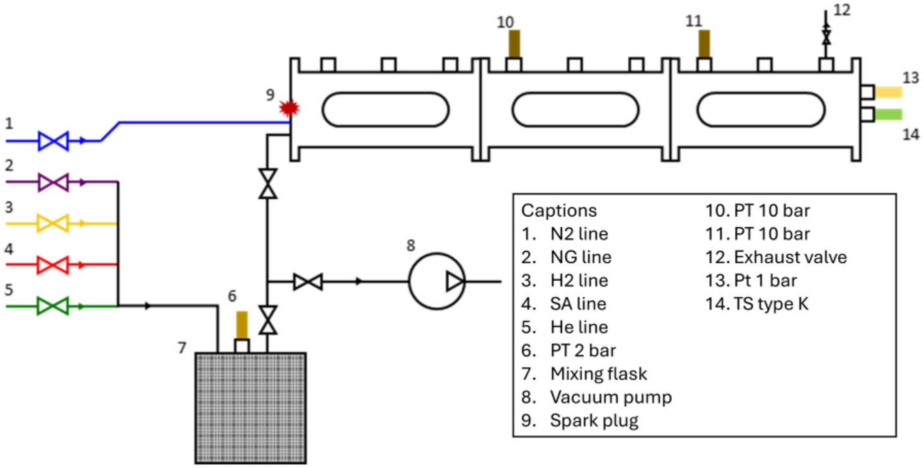

Fig. 1 Schematic representation of the experimental facility

lines to produce other mixtures. The NG considered to produce the experimental results used in this study had a composition of 90.8% CH4, 6% C2H6, 1.2% C3H8, 0.5% CO2, and 1.55% N2.

The mixing chamber consists of a 20 liter borosilicate spherical vessel, which is housed in a steel box for safety. The gas mixture was prepared following the partial pressure method using a 2 bar pressure transducer. The final pressure of the mixture inside the mixing chamber was 180 kPa. To prepare the mixture, the vacuum pump was first operated to bring the pressure inside the vessel to 0.5 kPa (or less). The NG was then added to the desired partial pressure and then air was added up to the final pressure. The gas mixture was then allowed to homogenize for at least 20 minutes. The uncertainty of the equivalence ratio was calculated according to the methodology described in (Quines da Silva et al. 2023) and a value of ±0.0291 was estimated.

The propagation duct consists of three modules with a 10 cm hydraulic diameter (D_h), a 10 cm x10 cm cross section and a duct length of 35 cm, each equipped with visualization windows. Each window has a size of about 10 cm x 6 cm, providing clear optical access to capture the flame evolution across successive sections of the duct. Therefore, the entire channel has a length of 105 cm. Once the mixture was ready, the vacuum pump brought the pressure inside the duct to 0.5 kPa (or less) before letting the mixture in. Notice that the mixture filled the duct to an initial pressure of 40 kPa. This initial pressure was selected based on safety considerations, as higher pressures could lead to excessive flame acceleration and pressure rise, potentially compromising the structural integrity of the visualization windows. Furthermore, the overall flame dynamics and acceleration trends are not expected to change significantly for initial pressures up to 100 kPa. The ignition source (8 kV and 30 mA) was then activated and the test was recorded by the high-speed video camera at 29,000 fps. The mixture was tested at least six times for each obstacle configuration, so at least two tests were recorded for each window.

The hydraulic inner and outer diameters of the obstacles were 4.8 cm, and 9.6 cm respectively, resulting in a blockage ratio (BR) of 75. The obstacles had two different configurations, namely a separation distance of 1 D_h and 1.5 D_h between the obstacles. A total of five obstacles were used in each case. Flame velocities were determined by processing the video recordings with the Tracker software (Brown et al. 2023). Repeatability of the experimental results is shown in Fig. 2, where the flame-tip position is plotted as a function of time, the position is expressed in reduced coordinates using x/S and the time is expresed in milliseconds. The laminar flame velocity (sL) was determined using Cantera (Goodwin et al. 2021) in conjunction with the San Diego chemical kinetic mechanism (USCD 2023). Note that, for the sake of brevity, in experimental terms, only the first configuration featuring a separation of 1 D_h between obstacles is discussed here. These experimental results were used to verify the numerical model used in this work.

3 Mathematical and Numerical Modeling

Both mathematical and numerical models employed in this work are briefly described in this section.

3.1 Governing Equations and Numerical Scheme

In this work, numerical simulations were carried out using PeleC (Henry de Frahan et al. 2022), an open-source, adaptive mesh refinement (AMR)-based solver for compressible reacting flows. This solver has previously been used in several DNS studies involving reactive compressible flows (Ramachandran et al. 2023; Sitaraman et al. 2021). The numerical simulations performed here involved the solution of the fully compressible, two-dimen-

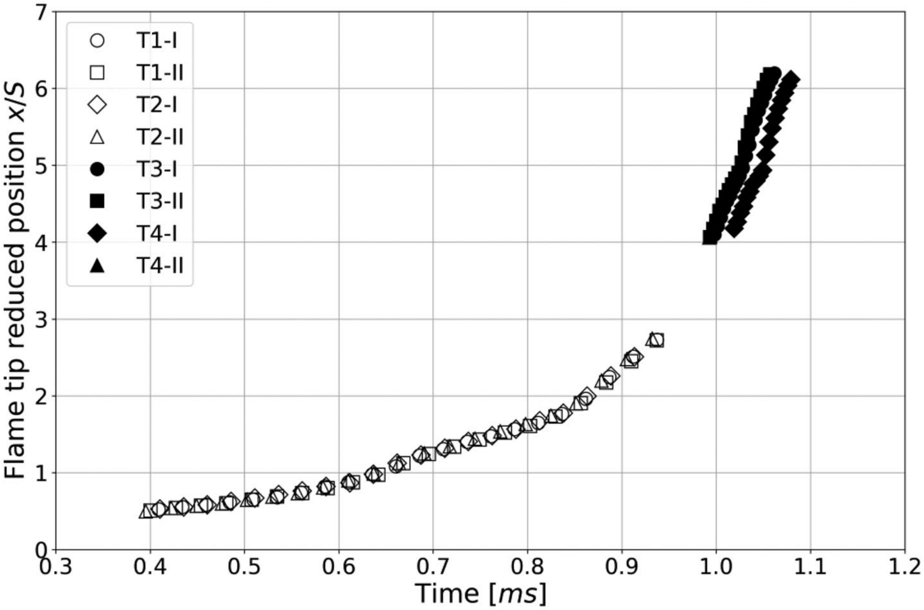

Fig. 2 Reproducibility of the experimental results for the case S = 1 D_h . Empty symbols correspond to the tests in window 1 and filled symbols to the tests in window 2

sional (2D), reactive Navier-Stokes equations, accounting for the conservation of mass, momentum, species, and energy,

$$\frac{\partial}{\partial t}(\rho) + \nabla\cdot(\rho\vec{u}) = 0 \tag{1}$$

$$\frac{\partial}{\partial t}(\rho\vec{u}) + \nabla\cdot(\rho\vec{u}\otimes\vec{u}) + \nabla p = -\nabla\cdot\Pi \tag{2}$$

$$\frac{\partial}{\partial t}(\rho Y_k) + \nabla\cdot(\rho\vec{u}Y_k) = -\nabla\cdot\mathcal{F}_k + \rho\dot{\omega}_k \tag{3}$$

$$\frac{\partial}{\partial t}(\rho E) + \nabla\cdot(\rho\vec{u}E + p\vec{u}) = \nabla\cdot Q - \nabla\cdot(\Pi\cdot\vec{u}) \tag{4}$$

with a finite-rate evaluation of chemistry in the compressible flow regime. In Eqs. (1)-(4), $\rho, \vec{u}, Y_k, t, \dot{\omega}_k, p,$ and E stand for density, velocity, -th chemical species mass fraction, time, k-th chemical species reaction rate, pressure, and total energy, respectively. The viscous stress tensor, under the Newtonian assumption, is given by,

$$\Pi = \eta\left(\nabla\vec{u} + (\nabla\vec{u})^T\right) + \left(\kappa - \tfrac{2}{3}\eta\right)\nabla\cdot\vec{u} \tag{5}$$

where η is the shear viscosity and κ is the bulk one. $\mathcal{F}_k$ is in turn the diffusive transport flux of the k-th chemical species and $\mathcal{Q}$ is the thermal conduction heat flux. To close the system involving the compressible Navier-Stokes equations, the ideal gas equation of state is employed. In addition, to describe the associated combustion processes, a 2-step CH4/air chemical kinetic reduced mechanism (Table 1), available in the PeleC libraries (Henry de Frahan et al. 2022), has been utilized. This kinetic mechanism has been selected here because previous studies (Valiev et al. 2010; Kessler et al. 2010; Gamezo et al. 2021) have shown that reduced mechanisms can provide a reasonable approximation of the key length and time scales characterizing deflagration-to-detonation transition (DDT) in methane–air combustion processes.

The numerical schemes employ a second-order explicit method-of-lines (MOL) approach for time advancement, utilizing a standard predictor-corrector method. The advective terms are computed using the MOL framework with slope limiting, while characteristic extrapolation in each direction is applied to compute left and right states at cell faces, which are inputs to the Riemann problem. This method supports complex geometries through the Embedded Boundary formulation. Diffusive terms are discretized in space using a straightforward, centered finite-volume scheme. Stiff chemical reactions are integrated using the CVODE method (Cohen et al.). The transport and time-averaged chemistry source terms are incorporated into a global second-order Runge-Kutta time-stepping framework, operating with a fixed CFL number of 0.2. Regarding the computational costs, notice that to complete the numerical simulation of the case with S = 1.5 D_h, about nine days of wall-clock time was required, which corresponds to about 13,824 CPU hours. All simulations were executed on

Table 1 Rate constants for the 2-step chemical kinetic reduced mechanism of CH4/air

Reactions	A	b	Ea
2 CH4 + 3 O2 → 2 CO + 4 H2O	1.545e + 14	0.5	3.9895e + 04
2 CO + O2 → 2 CO2	1.991e + 14	0.0	4.0e + 04
2 CO2 → 2 CO + O2	2.5e + 08	0.0	4.0e + 04

a single workstation equipped with an AMD Ryzen Threadripper PRO 7985WX processor featuring 64 physical cores and operating at a base frequency of 3.2 GHz. Full parallel utilization of all CPU cores was maintained throughout the entire numerical simulations to ensure computational efficiency.

3.2 Computational Domain and Boundary and Initial Conditions

As illustrated in Fig. 3, the computational domain encompasses a 2D obstructed channel, scaled down by a factor of 0.5 from the experimental setup, resulting in final domain dimensions of 2.5 cm × 52.5 cm. This downscaling was introduced to balance computational cost with physical resolution, allowing for finer grid resolution across the flame front while keeping the overall computational burden within practical limits. By reducing the physical size of the domain while preserving key non-dimensional parameters, the numerical simulations retained the dominant physics of flame acceleration and obstacle–flame interaction.

Following previous studies that suggest symmetry conditions in similar obstructed flame configurations (Gamezo et al. 2007, 2021), the numerical simulations performed in this work involve only half of the channel. More specifically, the channel is closed at x = 0 cm and x = 52.5 cm at the left and right ends, respectively. Along the ends and the bottom plane at y = 0 cm, a non-slip, adiabatic wall condition is applied, whereas the upper boundary at y = 2.5 cm is treated as a symmetry plane. In numerical simulations, the channel is filled with a stoichiometric CH4/air mixture with an initial pressure of 40 kPa. For flame ignition, as shown in Fig. 3, a hot zone area (3000 K) is initially placed on the left wall in the symmetry plane.

3.3 Computational Mesh

Accurate grid resolution at the flame front is crucial to properly modeling flame acceleration and DDT phenomena (Kessler et al. 2010). A sound practice in the literature to define the mesh resolution is to physically estimate the number of points across the flame thickness (Ramachandran et al. 2023). In this work, the thickness of the laminar flame thickness x_f has been estimated using Cantera (Goodwin et al. 2021), which represents a premixed 1D flame. Thus, the x_f obtained based on the temperature gradient resulted in a value equal to $x_f = 0.0914$ cm. In the work of Kessler et al. (Kessler et al. 2010), which involved a stoichiometric CH4/air mixture and a flow configuration similar to the one studied here, 5 cells per laminar flame thickness were used. In contrast, here, a grid resolution study was conducted involving different minimum grid sizes dx_{min}, determined based on the number of AMR levels. Specifically, the number of AMR levels determined by the temperature gradients was set equal to 0, 1, and 2. Consequently, the mesh size without AMR (AMR 0)

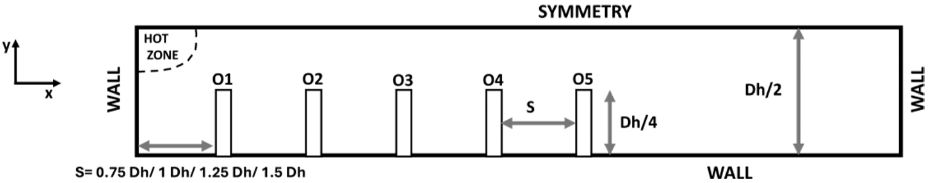

Fig. 3 Computational domain and boundary conditions. Obstacles are evenly spaced along the closed channel

featured a $dx_{min} = 0.01562cm$(~6 cells across the thickness of the flame), the one with 1 level of AMR (AMR 1) featured a $dx_{min} = 0.0078$ (~12 cells across the flame thickness), and the mesh with 2 levels of AMR (AMR 2) a $dx_{min} = 0.0039$ (~24 cells across the flame thickness).

The numerical results obtained using three different computational meshes are compared in Fig. 4 in terms of flame tip velocity (left) and flame tip reduced position (right). Specifically, the left plot presents the spatial evolution of the flame tip velocity as a function of the flame tip reduced position (x/S), while the right plot shows the corresponding evolution of the flame tip reduced position (x/S) over time. Experimental data for the case featuring a S = 1 D_h are included in both plots for reference. To allow a consistent comparison with the experimental results, it is important to emphasize here the treatment of each variable carried out. For the flame tip reduced position versus time (Fig. 4, right), no additional data scaling was required. Since the flame tip reduced position is normalized by the obstacle separation distance S, the resulting non-dimensional quantity inherently accounts for geometric scaling, and when plotted against time in milliseconds it shows a relatively good agreement with the experimental measurements. In contrast, to compare the flame tip velocity (Fig. 4, left), it was necessary to scale down the experimental velocity data by a factor of 2. This is because the experimental velocity was derived directly from the difference in flame tip positions between two snapshots over a fixed time interval, without accounting for the geometric downscaling present in the numerical setup. Therefore, scaling down the experimental velocity by a factor of 2 compensates for the reduced computational domain length accounted for in the numerical simulations and yields a consistent basis for comparison.

Accordingly, as observed in Fig. 4, increasing the level of mesh refinement, i.e., advancing from AMR 0 to AMR 2, leads to a noticeable improvement in the accuracy of the numerical predictions. In particular, the AMR 0 case significantly underpredicts both the flame tip velocity and its reduced position, reflecting insufficient resolution at the flame front. In contrast, AMR 1 and AMR 2 results show similar qualitative trends, with AMR 2 providing a slightly better match with experimental data, especially in the later stages of propagation. The increase from AMR level 0 to 1 yields a substantial improvement in the predicted flame tip velocity, whereas further refinement from level 1 to 2 results in marginal changes only. Based on this analysis, the mesh with two levels of adaptive mesh refinement (AMR 2), featuring a minimum cell size of $dx_{min} = 0.0039$ (corresponding to approximately 24

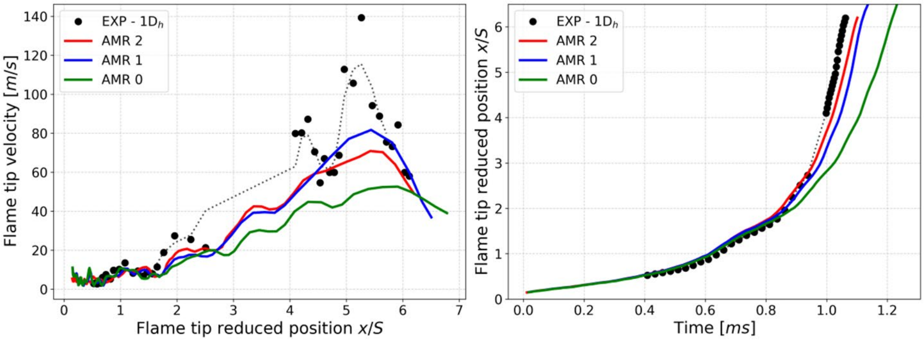

Fig. 4 Flame tip velocity (left) and flame tip reduced position (right) for grids with different AMR levels. Symbols: experimental, dotted lines: experimental data smoothed using a Gaussian filter, solid lines: numerical

grid points across the laminar flame thickness), is deemed sufficient for accurately capturing the relevant flame dynamics. Therefore, all numerical results discussed in this work are obtained using the AMR 2 mesh.

Fig. 5 presents in turn a comparison between experimental and numerical results for flame tip velocity (left) and flame tip reduced position (right) for two different obstacle separation distances, $S = 1.0\ D_h$ and $S = 1.5\ D_h$. In this figure, experimental data are shown using symbols, while numerical predictions are represented by solid. Fig. 5 left plot displays the flame tip velocity as a function of the flame tip reduced position (x/S), and the right one shows the flame tip reduced position (x/S) as a function of time. For the case with $S = 1.0\ D_h$, the numerical results show a relatively good agreement with the experimental data in both velocity magnitude and profile trends. However, for the case with $S = 1.5\ D_h$, clear discrepancies between numerical and experimental results are observed. Indeed, the numerical flame tip velocity underpredicts the experimental values, particularly beyond the third obstacle. This divergence increases with time, as seen in the Fig. 5 right plot, where the simulated flame lags behind the experimental flame front. The observed discrepancies are attributed here to limitations of the 2D numerical model employed, which does not fully capture the three-dimensional flow features and flame wrinkling characterizing the experiments. Moreover, the lower channel blockage ratio used in the numerical simulations (50%) compared to the experiments (75%) likely reduces the flame surface area and vorticity generation, leading to slower flame acceleration predictions. The results shown in Fig. 5 highlight the challenges of replicating experimental behavior in simplified computational domains like the one used in this work. Thus, to ensure consistency and avoid misleading comparisons with experimental data, the influence of obstacle separation distance on flame acceleration in obstructed channels is studied here in numerical terms only.

Knowing the limitations of the use of two-dimensional computational domains, it is somewhat unexpected that the predicted temporal evolution of the flame tip reduced position for the case with $S = 1.0\ D_h$ (Fig. 5, right) shows a relatively good agreement with the experimental data. This agreement here is likely because, for smaller obstacle spacing, the influence of three-dimensional effects such as transverse flame wrinkling and vortex stretching is less dominant. That is, for $S = 1.0\ D_h$, the flow remains more constrained and quasi two-dimensional, allowing the simplified model to capture more accurately the flame propagation dynamics. However, it is clear that the same does not occur for greater obstacle

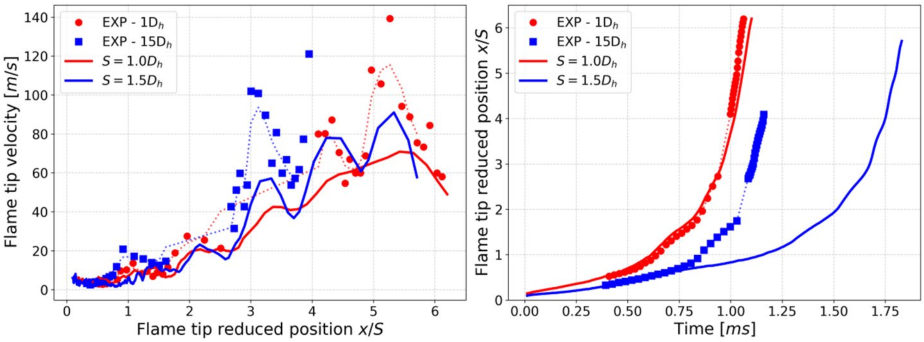

Fig. 5 Flame tip velocity (left) and flame tip reduced position (right) for 2 cases $S = 1\ D_h$ and $S = 1.5\ D_h$. Symbols: experimental, dotted lines: experimental data smoothed using a Gaussian filter, solid lines: numerical

separation distances. For the case with $S = 1.5\ D_h$ for instance, the results shown in Fig. 5 (right) highlight a clear discrepancy between simulations and experiments, confirming that the limitations of 2D approaches become more pronounced as the flow geometry becomes less confined.

4 Results and Discussions

The main results obtained in this work are highlighted in this section. These results include discussions about flame structure, flame dynamics, pressure dynamics, and interactions between vorticity and heat release.

4.1 Flame Structure

As shown in Fig. 6, the flame structures observed in both the experiments and the numerical results obtained in this work for the case with $S = 1\ D_h$ exhibit qualitative similarities in terms of flame progression and large-scale features. However, there are differences in flame shape and fine-scale structures between the experimental and the numerical results. In particular, the numerical results—based on a two-dimensional, scaled-down domain—cannot reproduce some three-dimensional effects observed experimentally, such as transverse flame wrinkling, asymmetric vortex development, and small-scale instabilities. These discrepancies are especially evident in the regions downstream of the fifth obstacle, where the experimental flame exhibits a more irregular and complex structure that is only partially captured by the numerical simulations carried out.

Notice that the experimental results shown in Fig. 6 were obtained using Schlieren imaging, while the numerical results are based on the computed density gradient from PeleC (Henry de Frahan et al. 2022). Due to the limited field of view in the experimental setup,

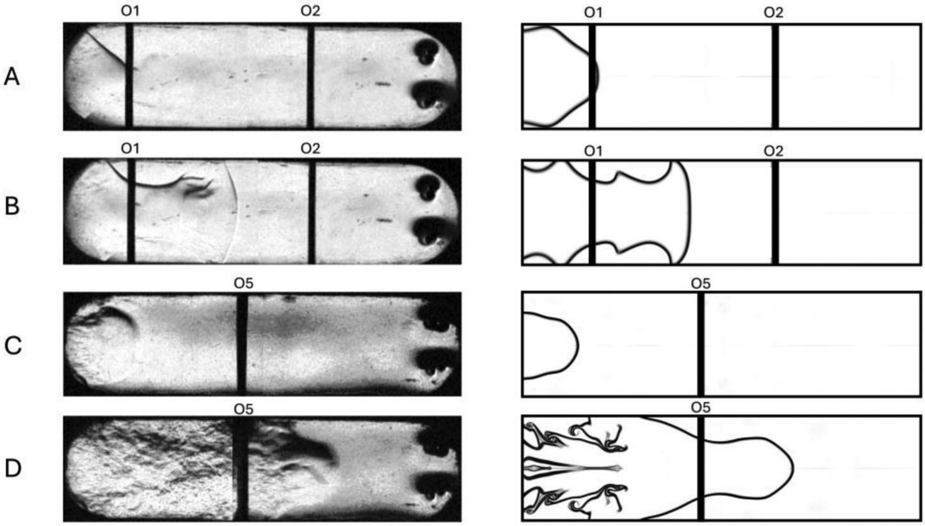

Fig. 6 Flame structure at different times, **A**) 12.8 ms **B**) 15.7 ms, **C**) 21.3 ms, and **D**) 22.2 ms. Experiments (left) vs PeleC numerical results (right) for $S = 1\ D_h$

which includes only two visualization windows, direct comparisons between numerical and experimental results are feasible only at positions close to the first two obstacles and to the last one. Accordingly, Fig. 6-A shows a snapshot of the flame as it approaches the first obstacle, where both the experimental and numerical data capture the jetting effect caused by flow constriction. In Fig. 6-B, the flame tip is located between the first and second obstacles. In both experimental and numerical snapshots shown in Fig. 6-B, the flame expands radially, indicating similar overall behavior. However, in Fig. 6-C and Fig. 6-D (just before and after the fifth obstacle, respectively), discrepancies between experimental and numerical results become more pronounced. The experimental flame structure appears significantly more wrinkled, with a large number of small-scale vortical structures. The numerical simulation in turn, while capturing the overall flame expansion and vortex formation, lacks resolution and dimensional fidelity to fully reproduce the complex flow structures observed in the experiments.

Fig. 7 illustrates in turn three different instants of the flame evolution during the second and third obstacle for $S = 1\ D_h$. Overall, the flame evolution in between obstacles can be split into three critical stages. In the first stage (Fig. 7, top), due to the contraction of the non-obstructed flow region, the obstacle jets out the flame to the unburnt gas. In the second stage (Fig. 7, center), the flame front stretches along the streamwise direction as it interacts with the large-scale recirculation zone behind the obstacle. As shown in Fig. 13, this second stage is strongly dependent on the obstacle separation distance S, as discussed further in Section 4.2 Finally, in the third stage (Fig. 7, bottom), the flame expands radially and interacts with vortices downstream of the obstacles, which distort the flame front and increase its local surface area (Han et al. 2020; Ciccarelli et al. 2005; Ibrahim et al. 2001).

4.2 Flame Dynamics

Notice first that, in all figures discussed in this Sect. 4.2, the horizontal axes represent the flame tip reduced position variable x/S, where xstands for the flame tip axial position and S is the obstacle separation distance. The use of this x/S variable allows for a clearer and more systematic comparison of the influence exerted by each obstacle on the flame dynamics and the associated flow characteristics across different S-based cases. The limits of the horizontal axes have been made uniform so as to cover the range [0, 6], such that the flame tip reduced positions 1 through 5 correspond to the locations of the five obstacles along the obstructed channel accounted for in this work.

Accordingly, Fig. 8 shows the numerical predictions of the flame-tip velocity corresponding to each of the four S-based cases studied in this work. The flame tip is computed here as the closest point of the reaction zone to the channel right end wall. Overall, larger separation distances (e.g., $S = 1.25\ D_h$) lead to faster flame accelerations with strong velocity oscillations (Zheng et al. 2023). This trend is attributed to longer residence times between obstacles, which allow the flame to undergo radial expansion and interact with instabilities likely associated with shear-layer development. For smaller spacings ($S = 0.75$ and $1\ D_h$), the flow confinement prevents flame full radial expansion, resulting in more constrained jet-like flame propagation dominated by axial stretching (Johansen and Ciccarelli 2013). Therefore, velocity oscillations become more prominent as S increases. For instance, during the third and fourth obstacles, for $S = 1.25$ and $1.5\ D_h$, the velocity reductions (V_{min}/V_{max}) are 0.84 and 0.64 respectively, indicating stronger oscillations. It is worth noticing that, after

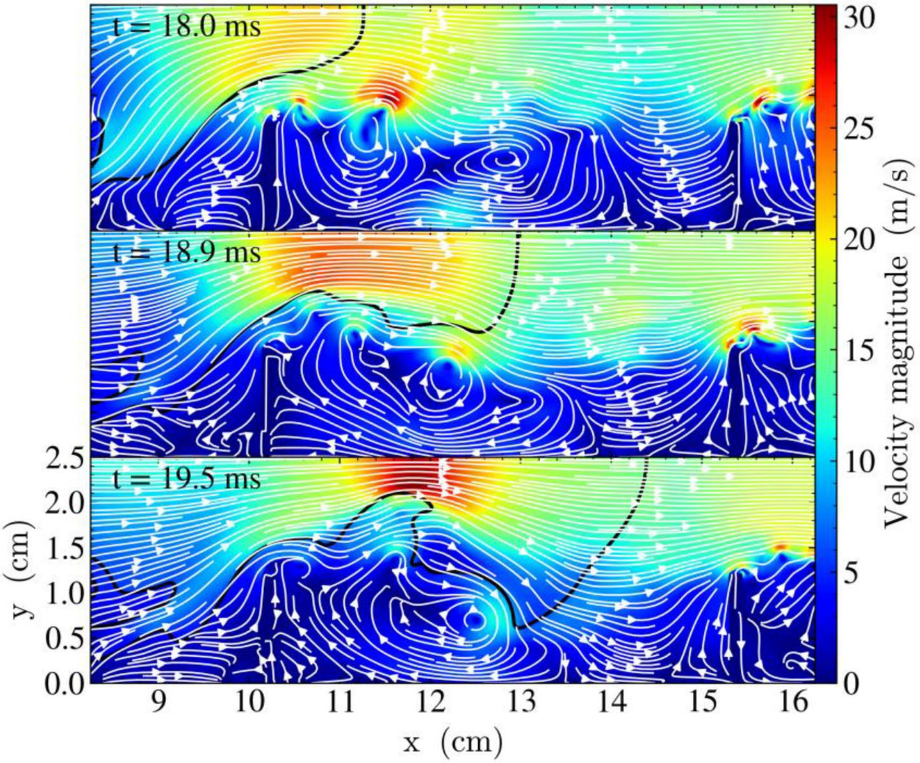

Fig. 7 Snapshots of flame front at three different times, 18.0 ms, 18.9 ms, and 19.5 ms, for S = 1 D_h. Black contours denote flame fronts, and white streamlines illustrate flow field structures. Velocity magnitude contours are displayed in the background

Fig. 8 Displacement velocity of the leading flame tip versus flame tip location for four different separation distances (S)

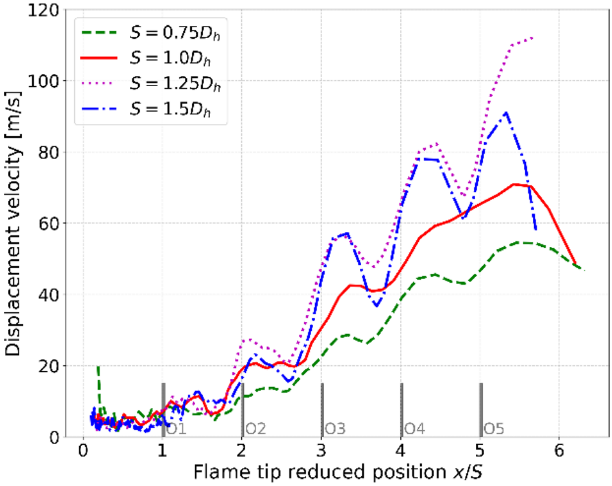

the fourth obstacle, the propagation velocity for S = 1.25 D_h ($\sim 84\ m/s$) surpasses the one with S = 1.5 D_h ($\sim 78\ m/s$) and this difference is more pronounced after the fifth obstacle ($\sim 115\ m/s$ and 91 m/s for S = 1.25 and 1.5, respectively). This finding suggests that, up to certain separation distance (around 1.25 D_h), the longer flame residence time promotes additional flame acceleration mechanisms, such as those related to vortices-flame interactions. Beyond this obstacle spacing however, further increases in S appear to diminish the effectiveness of the referred flame acceleration mechanisms.

Fig. 9 presents in turn the total flame surface area as a function of the flame tip reduced position x/S. A clear correlation between obstacle spacing and flame surface growth is observed. For instance, at the fifth obstacle, the flame surface area reaches about 122, 120, 60, and 43 cm for S values equal to 1.5, 1.25, 1, and 0.75 D_h, respectively. These surface area related differences arise from variations in vortex–flame interactions and the development of flow recirculation zones, as discussed in Sect. 4.3 (Johansen and Ciccarelli 2009). It is worth noticing here that, although the cases with S = 1.25 and 1.5 D_h exhibit similar trends in flame surface growth up to the fourth obstacle, the case featuring a S = 1.5 D_h shows a sharp spike in flame surface area afterward, suggesting a delayed but more intense vortex–flame interaction. In addition, Fig. 10 illustrates the cumulative heat release within the reaction zone. According to the obtained results, for smaller obstacle spacings (S = 0.75 and 1 D_h), heat release increases linearly along the channel, consistent with limited flame deformation and slower propagation. Conversely, for larger spacings (S = 1.25 and 1.5 D_h), the heat release exhibits exponential growth, particularly after the second and fourth obstacles. The S = 1.5 D_h heat release profile is the fastest growing, although it also shows more irregularities, suggesting a more chaotic vortex–flame interaction regime.

Fig. 11 depicts the spatial evolution of the magnitude of flow vorticity, a key indicator of rotational flow and vortex–flame interactions. From this figure, as the flame progresses, vorticity increases for all flow configurations studied here, but its intensity and variability depend strongly on the obstacle spacing. For instance, for S = 1.25 and 1.5 D_h the vorticity magnitude increases notably compared to the more confined cases, reaching values up to about three times higher. This confirms that larger obstacle separations allow the development of stronger and more complex vortical structures. In particular, the curve for S = 1.25 D_h rises rapidly and consistently, reflecting a well-sustained coupling between flame and

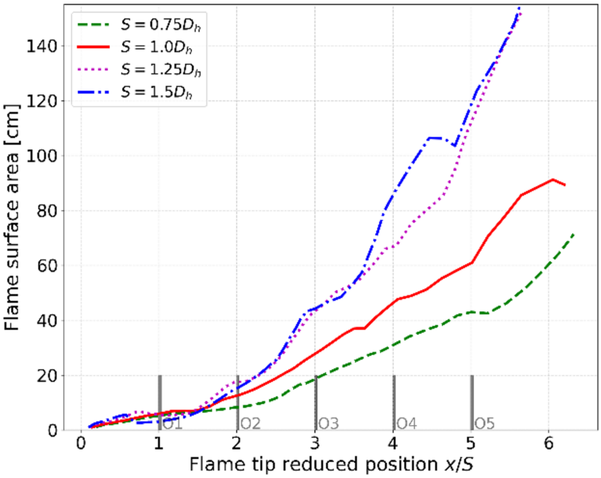

Fig. 9 Flame surface area versus flame tip location for four different separation distances (S)

Fig. 10 Average heat release versus flame tip location for four different separation distances (S)

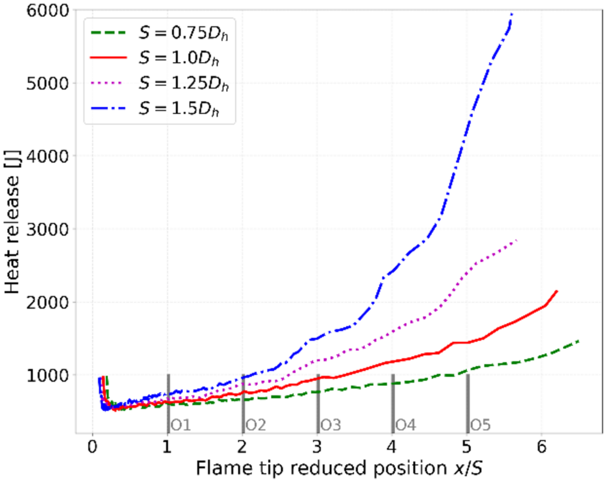

Fig. 11 Vorticity magnitude versus flame tip location for four different separation distances (S)

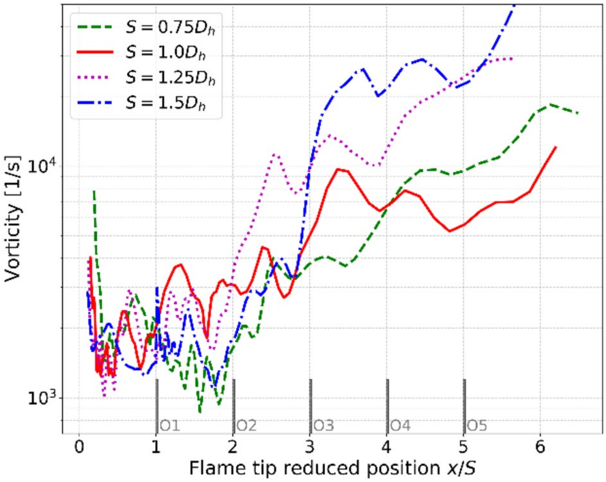

vortices, while the S = 1.5 D_h case shows larger fluctuations, indicating intermittent coherence. Finally, Fig. 12 shows the baroclinic torque, which quantifies the vorticity generation arising from the misalignment between pressure and density gradients—commonly linked to Rayleigh–Taylor instability (Zhou et al. 2021). In all S-based cases accounted for, the baroclinic torque increases as the flame propagates. For S = 1.25 and 1.5 D_h in particular, the baroclinic torque growth is substantial, especially after the fourth obstacle. The relatively high baroclinic torque observed for S = 1.5 D_h highlights a more unstable regime, although the effectiveness of this instability in promoting flame acceleration is reduced compared to the more organized flame dynamics seen for S = 1.25 D_h (Sect. 4.3).

Fig. 12 Baroclinic torque versus flame tip location for four different separation distances (S)

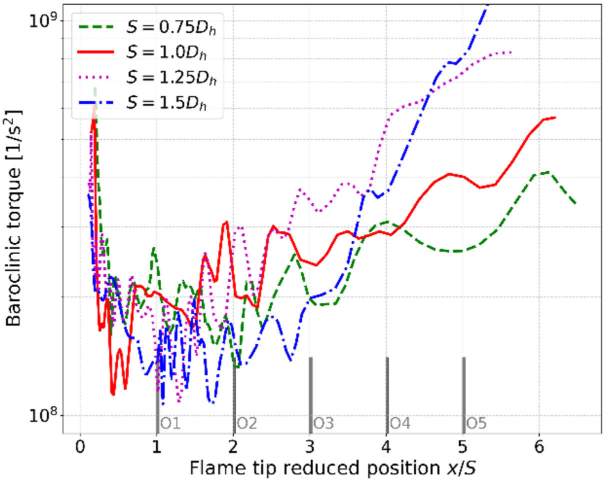

4.3 Flame Evolution and Flow Structure Downstream of Obstacles

Fig. 13 shows partially the temporal evolution of the flame structure as it propagates through the obstructed channel for the four obstacle separation distances (S) accounted for in this work. Specifically, downstream of the first obstacle, laminar roll-up vortices are formed due to flow induced by the expansion of combustion products (Johansen and Ciccarelli 2009). These vortices gradually evolve downstream, forming localized recirculation zones near the obstacle wakes. Notably, the vorticity magnitude in these small vortices increases significantly as the flame advances through the obstructed channel. For S = 1.0 D_h for instance, while the vorticity near the first obstacle is on the order of 5×10^3 s^{-1}, it rises to approximately 6×10^4 s^{-1} near the fifth obstacle—representing a 1-order-of-magnitude growth across the five-obstacle channel configuration.

The referred vortices play a critical role in flame acceleration, particularly during the second and third phases of the flame development process. In cases with small obstacle spacing (e.g., S = 0.75 D_h), the flame is highly confined and the flow between obstacles is strongly contracted. In these situations, axial elongation dominates the flame acceleration process. That is, the flame stretches quickly toward the next obstacle, but limited space and time inhibit the development of strong flow recirculation zones and flame radial expansion. As a result, vortex–flame interactions are relatively weak, and the flame surface remains relatively smooth. For S = 1.0 D_h, more defined vortical structures begin to appear downstream of the obstacles, although their interaction with the flame remains limited. The flow is still predominantly governed by axial motion, and even though some vortex penetration occurs, its influence on flame surface growth is moderate.

In contrast, the case with S = 1.25 D_h exhibits the most favorable conditions for flame acceleration. The increased obstacle separation allows indeed the flame to pass through all the flame acceleration stages, axial elongation, radial expansion, and strong vortex–flame interaction. Flow recirculation zones become more coherent and energetic, and the vortices are effectively coupled with the flame front. This leads to pronounced flame wrinkling, an increase in surface area (as shown in Fig. 9), and sustained flame acceleration. When the obstacle separation distance is further increased to S = 1.5 D_h, the vortices remain strong

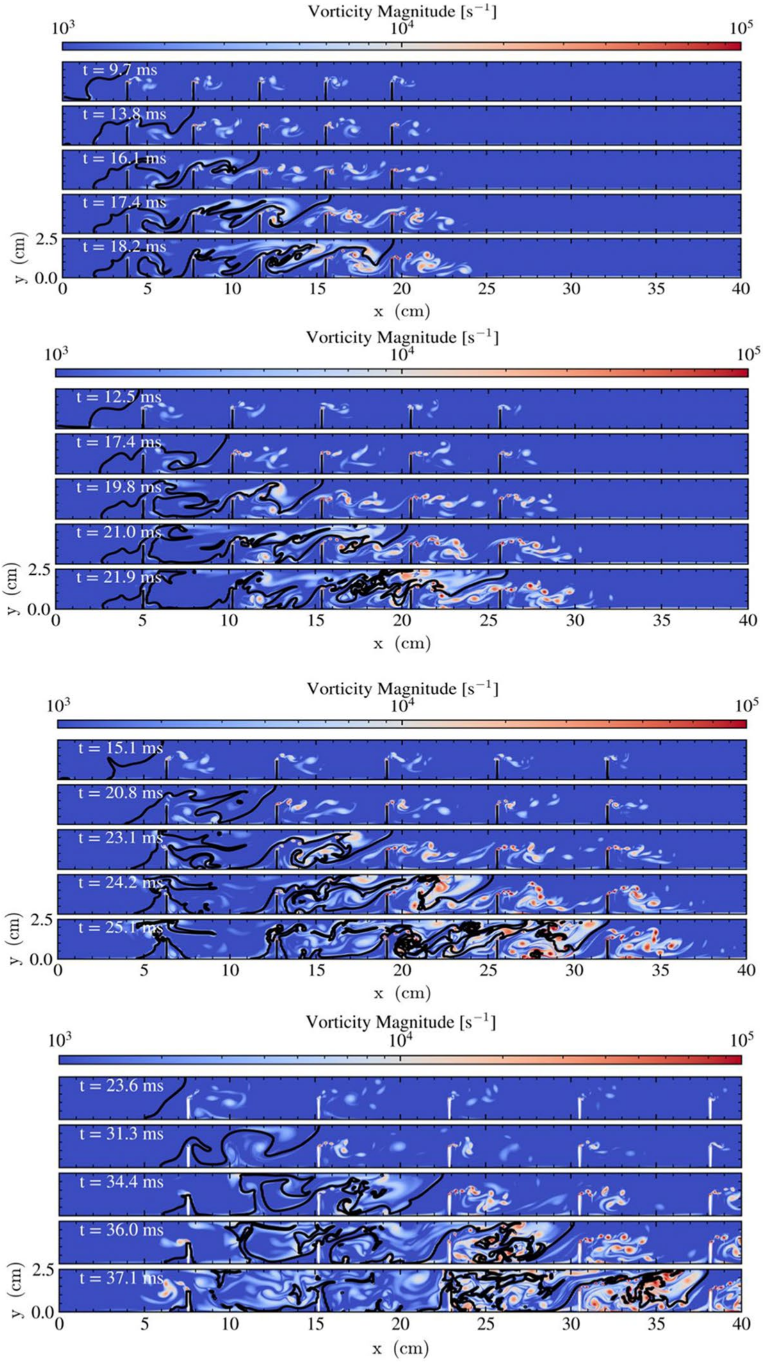

Fig. 13 Flame structure at different times for four obstacle separation distances, $S = 0.75\ D_h$ (top), $S = 1\ D_h$ (upper center), $S = 1.25\ D_h$ (bottom center), and $S = 1.5\ D_h$ (bottom). In these plots, the black lines denote the flame front, and the vorticity field is shown in the background

but become more scattered and less spatially coherent. Their alignment with the flame front weakens, particularly after the fourth obstacle, leading to partial decoupling between the flame and the flow recirculation zones. Although vortex–flame interactions are still present, their contribution to flame acceleration is reduced compared to the more optimal S = 1.25 D_h flow configuration. This suggests that, beyond a certain obstacle spacing, the increased flow residence time between obstacles is no longer beneficial, as it diminishes the strength of organized flame–vortex coupling. Overall, the numerical results obtained here indicate that the downstream flow dynamics and vortex evolution are highly sensitive to the obstacle separation distance. In particular, the flow configuration featuring S = 1.25 D_h exhibits the most sustained flame acceleration, driven by a clear sequence of flame elongation, flame radial expansion, and coherent vortex–flame interactions.

4.4 Pressure Dynamics

As discussed previously, for relatively large S values, the baroclinic torque around the last obstacles increases considerably (Fig. 12). These results agree with the experimental findings of Johansen et al. (Johansen and Ciccarelli 2009), who observed that the transition from low to high-speed flame propagation is marked by the formation of compression waves. Accordingly, Fig. 14 left plots display vorticity magnitude snapshots during flame propagation through the fourth and fifth obstacles for four values of S. Indeed, for S = 0.75 D_h (Fig. 14–A, left), vortex formation appears confined, with limited flame deformation due to the tight spacing between obstacles. In contrast, for S = 1.5 D_h (Fig. 14–D, left), the flame front interacts with intense and disordered vortical structures, indicating chaotic dynamics and loss of coherent vortex-flame coupling. Fig. 14 right plots show in turn the normalized pressure profiles ahead of the flame front along the channel centerline (y = 2.5 cm) during the flame's propagation through the fourth and fifth obstacles as well. Each colored curve in these Fig. 14 right plots represent a different temporal snapshot within this flame propagation interval, with timestamps indicated in the plot legends (e.g., for S = 0.75 D_h: 17.38 ms to 18.19 ms). Notice that at each of these time instants accounted for, the pressure was sampled along a line extending from the current flame tip position to a location 15 cm downstream. In addition, in Fig. 14 right plots, the black line with symbols represents the average of all these temporally pressure profiles, providing a reference for assessing pressure fluctuations.

Overall, the average pressure profiles exhibit an oscillatory behavior whose amplitude varies significantly with the obstacle separation distance S. For relatively small obstacle separation distances such as S = 0.75 D_h (Fig. 14–A), the pressure oscillations are relatively uniform, fluctuating around a mean value of approximately 52.7 kPa. In contrast, for S = 1.25 D_h (Fig. 14–C), the initial peak in the average pressure reaches about 70.0 kPa, followed by a slight decay to about 69.25 kPa farther downstream. For the largest spacing, S = 1.5 D_h (Fig. 14–D), the average pressure profile shows the highest-amplitude oscillations around 1 kPa.

As reported by Gamezo et al. (Gamezo et al. 2007; Emami et al. 2015), fast flame propagation is often associated with the formation of strong shock waves, which subsequently interact with the flame front and induce small-scale vortices. In this work, the increase in pressure ahead of the flame front shows a clear dependence on the obstacle separation distance S. For instance, in the case of S = 0.75 D_h (Fig. 14–A), the normalized pressure increases by only 0.07 between the earliest and latest time snapshots analyzed during flame

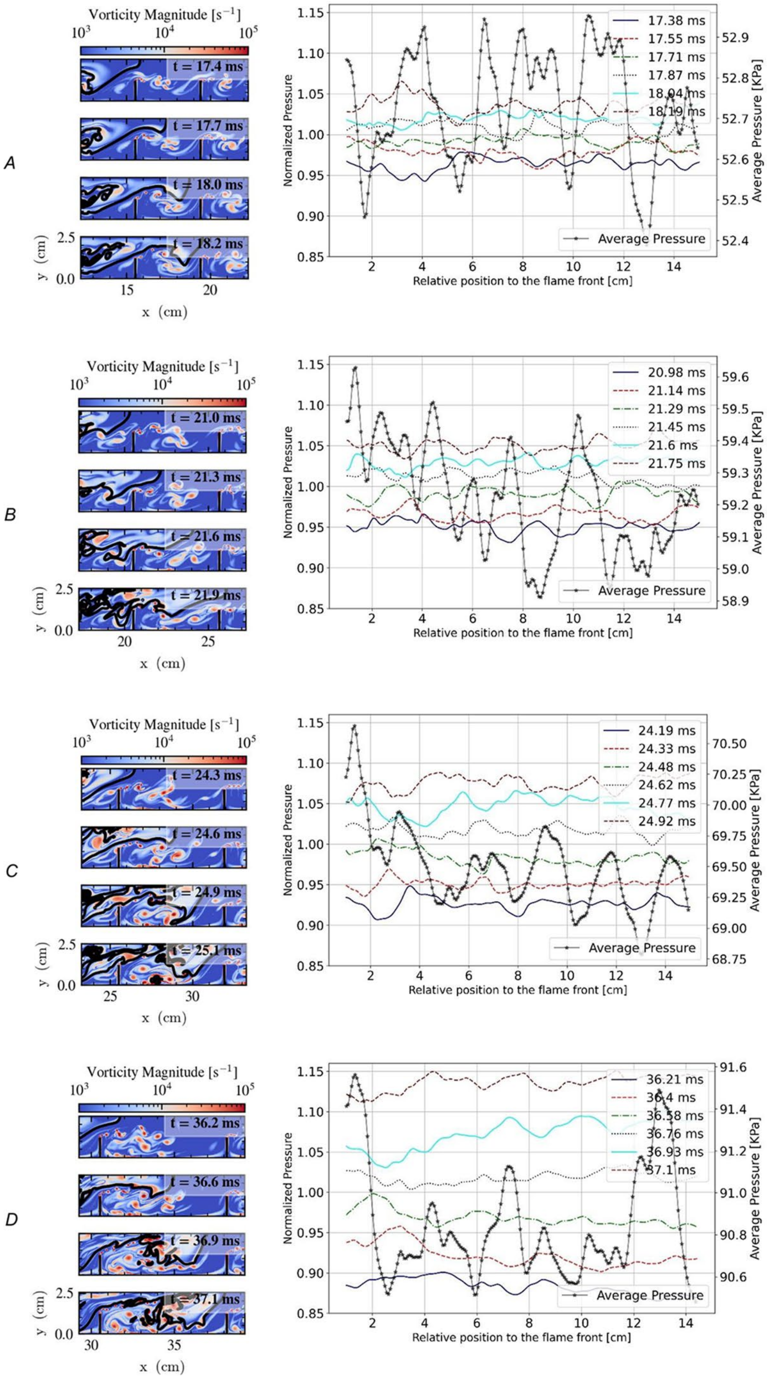

Fig. 14 Sequence of snapshots showing the magnitude of the vorticity field during the flame propagation through the fourth and fifth obstacles (left), and normalized pressure profiles ahead the flame front at different instants (right). Black lines with symbols: average pressure. Plots from top to bottom correspond to S = 0.75, S = 1, S = 1.25, and S = 1.5 D_h, respectively

propagation between the fourth and fifth obstacles, which corresponds to a physical pressure increase of approximately 3.6 kPa. In contrast, for $S = 1.5\ D_h$ (Fig. 14–D), the normalized pressure increases by about 0.25 over the same flame evolution interval, indicating a significantly stronger pressure buildup of approximately 22 kPa. This temporal growth in pressure is evident in the sequence of pressure profiles associated with each S-based case analyzed here, where later time profiles show progressively higher peak pressures compared to earlier ones.

Furthermore, the intensity of the pressure waves ahead of the flame front increases with the increase in the obstacle separation distance S. This is observed when analyzing for each S-based case the maximum normalized pressure amplitude, which is computed here by evaluating all pressure profiles (lines) accounted for. These maximum amplitudes, which reflect the spatial pressure oscillations caused by compression waves, are indeed about 0.023, 0.025, 0.025, and 0.026 for $S = 0.75\ D_h$, $1\ D_h$, $1.25\ D_h$, and $1.5\ D_h$, respectively. Although these pressure amplitudes are similar in normalized terms, due to the differences in average pressure characterizing each S-based case, their absolute values increase with S. Specifically, for $S = 1.5\ D_h$, physical pressure fluctuations reach up to 2.4 kPa, compared to approximately 1.21 kPa for $S = 0.75\ D_h$. These spatial pressure oscillations along each pressure line studied here highlight the intensity of the pressure waves interacting with the flame front.

4.5 Vorticity and Heat Release Interaction

Fig. 15 presents a sequence of snapshots showing the spatial distributions of heat release rate (left) and vorticity magnitude (right) during flame propagation through the fourth and fifth obstacles for the case with $S = 1.5\ D_h$. These snapshots corresponding to four different times illustrate the progressive transition from the flame axial elongation stage to the onset and intensification of vortex–flame interactions. During the flame axial elongation ($t = 36.2$ ms and 36.6 ms) indeed, there is reduced vortex-flame interaction, so the associated heat release is the lowest one of the flame acceleration cycles. As the flame enters the radial expansion stage ($t = 36.9$ ms), vortices begin to penetrate the reaction zone corrugating the flame surface. This interaction enhances local mixing and flame surface area, leading to a significant increase (~1500 J) in total heat release, from approximately $10^{3.6}$ to $10^{3.75}$ J. At later times (e.g., $t = 37.1$ ms), the vortex–flame interaction becomes more intense and chaotic. In addition, the heat release contours show highly corrugated flame fronts and several detached high-intensity reaction zones, indicative of strong local burning driven by vortex-induced flame folding. These effects are particularly pronounced for large obstacle spacing, such as $S = 1.5\ D_h$, where vortex coherence is diminished but vortex–flame interaction strength remains high. This chemistry–vorticity coupling highlighted in Fig. 15 is further discussed following the results shown in Fig. 16.

Accordingly, Fig. 16 presents the joint probability density function (J-PDF) of the logarithm of total heat release rate, $\log_{10}\left(\dot{Q}\right)$, and the logarithm of vorticity magnitude, $\log_{10}\left(\omega\right)$, evaluated in the vicinity of the flame front. These J-PDF are computed accounting for four different times, corresponding to the snapshots shown in the left plots of Fig. 14, which capture the flame propagation between the fourth and fifth obstacles. In Fig. 16, each row of plots represents a different obstacle separation distance (from top to bottom), $S = 0.75$, 1.0, 1.25, and 1.5 D_h. Besides, the values included in parentheses in each plot indi-

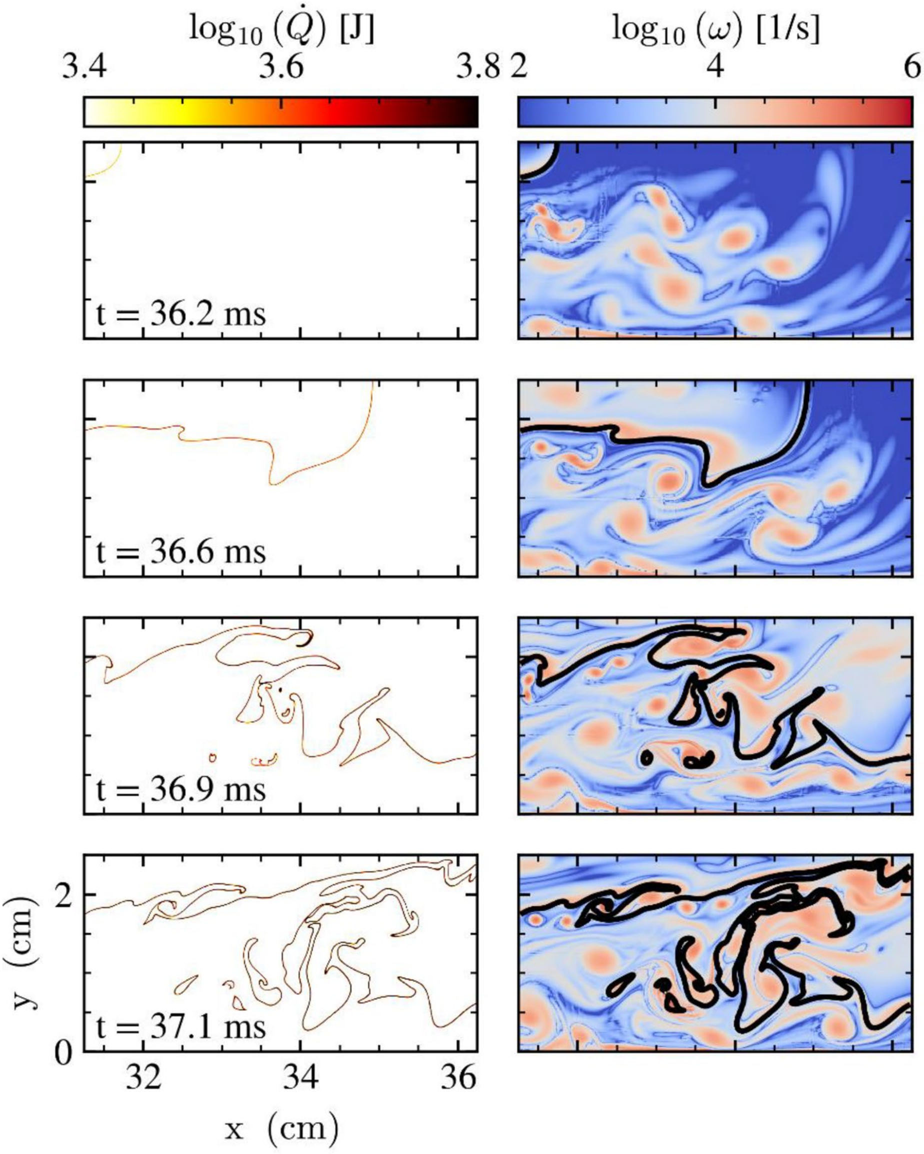

Fig. 15 Sequence of snapshots of heat release (left) and vorticity magnitude (right) for four different times during the flame propagation through the fourth and fifth obstacles for the case with S = 1.5 D_h

cate the location (vorticity and heat release-related coordinates) of the J-PDF peak values. Indeed, the plot regions featuring the J-PDF highest values highlight the most probable combination of local vorticity and heat release at a given time, revealing how vortex–flame interactions contribute to combustion intensification. As the flame accelerates, the location of the J-PDF peak values systematically shift toward higher $\log_{10}(\omega)$ and higher $\log_{10}(\dot{Q})$ values. This trend indicates that greater vortex strength is associated with more folded flame surfaces, which locally enhance chemical activity and energy release. As observed in Fig.

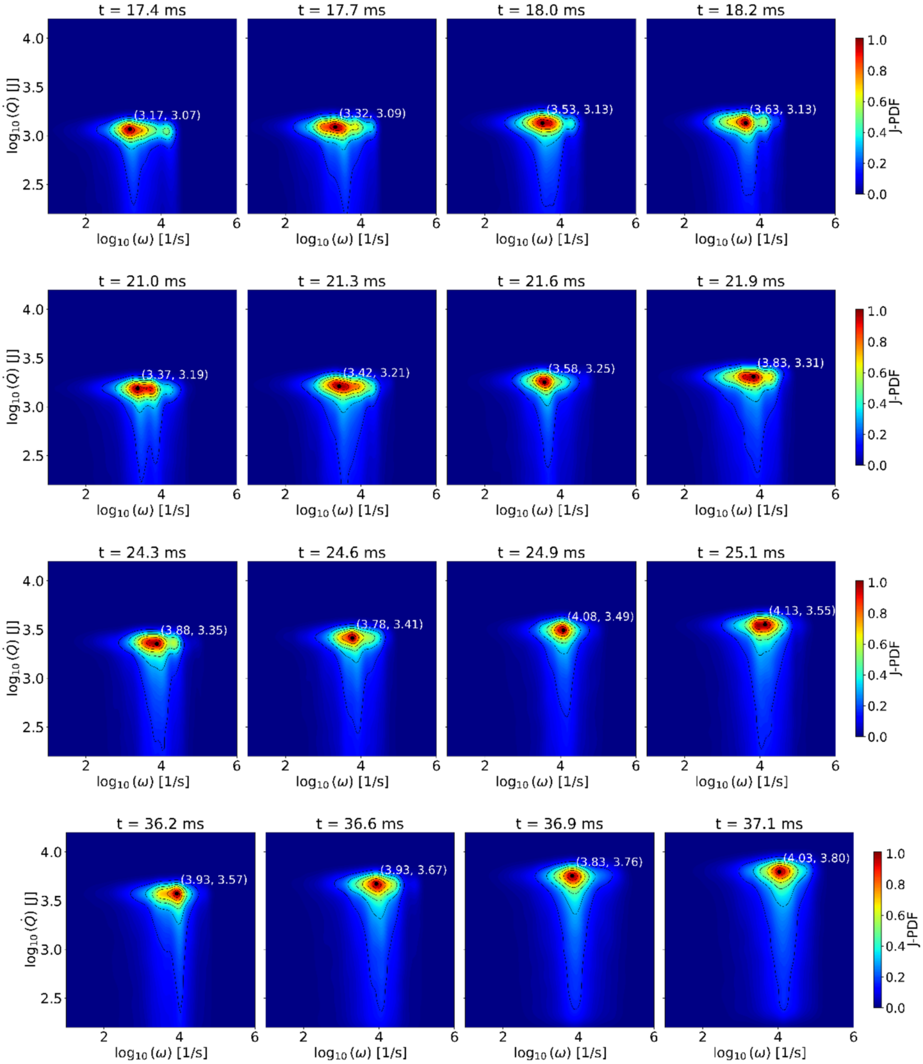

Fig. 16 Joint probability density function (J-PDF) of total heat release and vorticity magnitude within the reaction zone at four different times. Each dataset corresponds to the sequence of snapshots shown in the left plots of Fig. 14. The values included in parentheses in each plot indicate the location (vorticity and heat release-related coordinates) of the J-PDF peak values. Plots from top to bottom correspond to S = 0.75, S = 1, S = 1.25, and S = 1.5 D_h, respectively

15 for the S = 1.5 D_h case (e.g., t = 36.9 and 37.1 ms), regions of high vorticity coincide with intense flame wrinkling and elevated heat release, confirming this coupling.

Observing the results shown in Fig. 16, a clear pattern across different S values emerges, i.e., as the obstacle separation increases, the location of the J-PDF peak values shifts to higher values in both coordinate axes, emphasizing that larger S promotes stronger vortex–flame interactions. For instance, the J-PDF peak values moves from $\log_{10}(\omega) \approx 3.63$ and $\log_{10}\left(\dot{Q}\right) \approx 3.13$ at t = 18.19 ms for S = 0.75 D_h (Fig. 16, top right), to $\log_{10}(\omega) \approx 4.03$ and $\log_{10}\left(\dot{Q}\right) \approx 3.80$ at t = 37.10 ms for S = 1.5 D_h (Fig. 16, bottom right). Similarly, the cumulative vertical shift in $\log_{10}\left(\dot{Q}\right)$ between the first- and last-time instants for each S-based case—interpreted as an indicator of increased total heat release—is approximately 0.06, 0.12, 0.20, and 0.23 for S = 0.75, 1.0, 1.25, and 1.5 D_h, respectively. These values correspond respectively to physical increases in total heat release of ~ 174 J, 492 J, 1309 J, and 2594 J, showing that larger spacing promotes greater combustion intensification via vorticity increases. Interestingly, only in the S = 1.5 D_h case the vorticity magnitude does exhibit a drop between the second and third snapshots, that is, the peak value decreases from $\log_{10}(\omega) = 3.93$ (~8511 s^{-1}) at $t = 36.58$ ms to 3.83 (~6760 s^{-1}) at $t = 36.93$ ms. This behavior, not observed in other S-based cases, coincides with a more disordered vorticity field at later times. However, despite this local reduction in vorticity, the heat release continues to increase (from $\log_{10}\left(\dot{Q}\right) \approx 3.67$ to about 3.76), possibly due to enhanced mixing and flame surface area inherited from earlier flame–vortex interactions.

Overall, Fig. 16 confirms that flame–vortex interactions are a key driver of enhanced heat release during flame acceleration in obstructed channels. The spatial evolution of the J-PDF peak values illustrates how these interactions intensify and become more effective with increased obstacle spacing, up to a critical point. Beyond this point, as observed in the S = 1.5 D_h case, the loss of spatial coherence in the vorticity field may weaken the coupling with the flame, despite higher local vorticity. These results reinforce the idea that there exists an optimal separation distance—such as S = 1.25 D_h—that maximizes the constructive interaction between flame structures and flow instabilities.

5 Conclusions

This work presented a high-fidelity numerical investigation on the propagation of premixed methane–air flames in obstructed channels, focusing on the role of obstacle separation distance (S) in shaping the underlying physical mechanisms that control flame acceleration. 2-dimensional direct numerical simulations (DNS) were performed using the PeleC solver accounting for four different flow configurations (S = 0.75 D_h, 1 D_h, 1.25 D_h, and 1.5 D_h), enabling in this way a comprehensive analysis of flame-tip velocity, flame surface area, heat release rate, vorticity magnitude, baroclinic torque, and pressure dynamics.

The main results indicate that increasing obstacle separation induces a transition in the dominant flame acceleration mechanism—from geometry-driven jetting to instability-driven propagation. For relatively small obstacle separations, acceleration is governed primarily by flame axial elongation through narrow unobstructed gaps. This flow confinement limits flame radial expansion and suppresses vortex formation, resulting in smooth flame propagation, reduced flame surface area, and weak coupling with hydrodynamic instabilities. As the obstacle separation increases, the flame has sufficient time and space to undergo radial expansion and to interact with stronger vortices formed in the flow recirculation zones downstream of obstacles. This interaction enhances flame wrinkling, surface growth, and heat release. Indeed, the case with S = 1.25 D_h exhibits the most efficient coupling of flame acceleration mechanisms, with the flame tip velocity exceeding 115 m/s and the flame surface area reaching over 120 cm after the fifth obstacle. The joint probability density function (PDF) analysis between vorticity and heat release carried out reveals a clear statistical correlation between intense vortical regions and local peaks in energy release, underscoring the role of vortex-induced flame deformation in driving flame acceleration.

For the largest obstacle spacing ($S = 1.5\,D_h$) studied here, although both vorticity and flame surface area continue to grow, the coupling between vortices and flame becomes less coherent. The resulting flow is more chaotic, reducing the efficiency of flame acceleration. The peak flame velocity in this case is limited to about 91 m/s, and pressure wave amplitudes reach up to 2.4 kPa. Although moderate in absolute magnitude, such pressure waves—when sustained or reflected—may induce localized dynamic loading, especially in confined geometries or structurally sensitive components such as optical windows or thin-walled combustors. These findings highlight that obstacle separation distance is a critical design parameter for optimizing both performance and safety in combustion systems. Particularly, flow configurations with moderate spacing (e.g. $S = 1.25\,D_h$) promote controlled flame acceleration through well-coupled flame–vortex and pressure–flame interactions. In contrast, excessively large spacing (e.g., $S = 1.5\,D_h$) promotes the formation of stronger pressure waves and more chaotic flame dynamics, which may increase mechanical stresses and safety risks. From a structural design perspective, avoiding overly large obstacle spacing can help mitigate pressure peaks and oscillations, contributing to safer and more robust combustor configurations. Overall, this work provides new physical insight into the coupling between flame propagation and hydrodynamic instabilities in confined channels such the one accounted for here.

Acknowledgements Luis Bravo was supported by the DEVCOM Army Research Laboratory 6.1 basic research program in propulsion sciences. The computations were supported in part by CPUs at Purdue Anvil through allocation MCH240024 from the Advanced Cyberinfrastructure Coordination Ecosystem: Services & Support (ACCESS) program, which is supported by National Science Foundation grants #2138259, #2138286, #2138307, #2137603, and #2138296.

Author contributions S.V. conducted the investigation, developed the numerical methodology, performed software validation, and contributed to the original draft and formal analysis. F.I. handled visualization, formal analysis, and contributed to writing the original draft. L.A. designed and performed the experiments. A.M. supervised the project, contributed to the experimental methodology, reviewed and edited the manuscript, and secured funding. L.B. provided supervision, contributed to formal analysis and numerical methodology, reviewed and edited the manuscript, and handled project administration and funding acquisition. P.K. contributed to manuscript review and editing. C.C. conceptualized the study, developed the numerical methodology, supervised the project, reviewed and edited the manuscript, and handled project administration and funding acquisition. All authors reviewed and approved the final manuscript.

Funding Open access funding provided by Pontificia Universidad Catolica del Peru. This investigation was funded by the US Army Research Laboratory and the US Air Force Office of Scientific Research (AFOSR) under Research Grant No. W911NF-22-1-0275.

Data availability No datasets were generated or analysed during the current study.

Declaration

Competing interest The authors declare no competing interests.

References

Brown, D., Hanson, R., Christian, W.: Tracker video analysis and modeling tool. (2023)

Ciccarelli, G., Dorofeev, S.: Flame acceleration and transition to detonation in ducts. Prog. Energy Combust. Sci. **34**, 499–550 (2008). https://doi.org/10.1016/j.pecs.2007.11.002

Ciccarelli, G., Fowler, C.J., Bardon, M.: Effect of obstacle size and spacing on the initial stage of flame acceleration in a rough tube. Shock. Waves **14**, 161–166 (2005). https://doi.org/10.1007/s00193-005-0259-4

Cohen, S.D., Hindmarsh, A.C., Dubois, P.F.: CVODE, A Stiff/Nonstiff ODE Solver in C. Computers in Physics **10**, 138–143 (1996). https://doi.org/10.1063/1.4822377

Emami, S., Mazaheri, K., Shamooni, A., Mahmoudi, Y.: LES of flame acceleration and DDT in hydrogen-air mixture using artificially thickened flame approach and detailed chemical kinetics. Int. J. Hydrogen Energy **40**, 7395–7408 (2015). https://doi.org/10.1016/j.ijhydene.2015.03.165

Gamezo, V.N., Bachman, C.L., Oran, E.S.: Flame acceleration and DDT in large-scale obstructed channels filled with methane-air mixtures. Proceedings of the Combustion Institute **38,** 3521–3528 (2021). https://doi.org/10.1016/j.proci.2020.09.018

Gamezo, V.N., Ogawa, T., Oran, E.S.: Numerical simulations of flame propagation and DDT in obstructed channels filled with hydrogen-air mixture. Proceedings of the Combustion Institute **31**, 2463–2471 (2007). https://doi.org/10.1016/j.proci.2006.07.220

Goodwin, D.G., Speth, R.L., Weber, H.K.M., B.W.: Cantera: an object-oriented software toolkit for chemical kinetics, thermodynamics, and transport processes. (2021)

Hall, R., Masri, A., Yaroshchyk, P., Ibrahim, S.: Effects of position and frequency of obstacles on turbulent premixed propagating flames. Combust Flame **156**, 439–446 (2009). https://doi.org/10.1016/j.combustflame.2008.08.002

Han, S., Yu, M., Yang, X., Wang, X.: Effects of obstacle position and hydrogen volume fraction on premixed syngas-air flame acceleration. Int. J. Hydrogen Energy **45**, 29518–29532 (2020). https://doi.org/10.1016/j.ijhydene.2020.07.189

Henry de Frahan, M.T., Rood, J.S., Day, M.S., Sitaraman, H., Yellapantula, S., Perry, B.A., Grout, R.W., Almgren, A., Zhang, W., Bell, J.B., Chen, J.H.: PeleC: an adaptive mesh refinement solver for compressible reacting flows. Int. J. High Perform. Comput. Appl. **37**, 115–131 (2022). https://doi.org/10.1177/10943420221121151

Huang, C., Chen, X., Liu, L., Zhang, H., Yuan, B., Li, Y.: The influence of opening shape of obstacles on explosion characteristics of premixed methane-air with concentration gradients. Process Saf. Environ. Prot. **150**, 305–313 (2021). https://doi.org/10.1016/j.psep.2021.04.028

Ibrahim, S.S., Hargrave, G.K., Williams: T.C.: Experimental investigation of flame/solid interactions in turbulent premixed combustion. Experimental Thermal and Fluid Science **24**, 99–106 (2001). https://www.sciencedirect.com/science/article/pii/S0894177701000413

Johansen, C., Ciccarelli, G.: Modeling the initial flame acceleration in an obstructed channel using large eddy simulation. J. Loss. Prev. Process. Ind **26**, 571–585 (2013). https://doi.org/10.1016/j.jlp.2012.12.005

Johansen, C.T., Ciccarelli, G.: Visualization of the unburned gas flow field ahead of an accelerating flame in an obstructed square channel. Combust. Flame **156**, 405–416 (2009). https://doi.org/10.1016/j.combustflame.2008.07.010

Kessler, D.A., Gamezo, V.N., Oran, E.S.: Simulations of flame acceleration and deflagration-to-detonation transitions in methane-air systems. Combust. Flame **157**, 2063–2077 (2010). https://doi.org/10.1016/j.combustflame.2010.04.011

Kuznetsov, M., Ciccarelli, G., Dorofeev, S., Alekseev, V., Yankin, Y., Kim, T.H.: DDT in methane-air mixtures. Shock. Waves **12**, 215–220 (2002). https://doi.org/10.1007/s00193-002-0155-0

Liu, Z., Li, X., Li, M., Xiao, H.: Flame acceleration and DDT in a channel with fence-type obstacles: effect of obstacle shape and arrangement. Proceedings of the Combustion Institute **39**, 2787–2796 (2023). https://doi.org/10.1016/j.proci.2022.08.046

Na'inna, A.M., Phylaktou, H.N., Andrews, G.E.: The acceleration of flames in tube explosions with two obstacles as a function of the obstacle separation distance. J. Loss. Prev. Process. Ind **26**, 1597–1603 (2013). https://doi.org/10.1016/j.jlp.2013.08.003

Na'inna, A.M., Phylaktou, H.N., Andrews, G.E.: Effects of obstacle separation distance on gas explosions: the influence of obstacle blockage ratio. Procedia Engineering **84**, 306–319 (2014).

Park, D., Green, A., Lee, Y., Chen, Y.: Experimental studies on interactions between a freely propagating flame and single obstacles in a rectangular confinement. Combust. Flame **150**, 27–39 (2007). https://doi.org/10.1016/j.combustflame.2007.04.005

Quines da Silva, R., Lauermann, C.H., Nzinga, M.K., Dall Agnol, M., Cardoso, G.R., Mendiburu, A.Z.: Experimental and theoretical analyses of deflagrations of mixtures involving hydrogen enrichment and helium dilution inside a closed duct. Energy. Fuels **37** (2023). https://doi.org/10.1021/acs.energyfuels.3c02615

Ramachandran, S., Srinivasan, N., Wang, Z., Behkish, A., Yang, S.: A numerical investigation of deflagration propagation and transition to detonation in a microchannel with detailed chemistry: effects of thermal boundary conditions and vitiation. Phys. Of Fluids **35** (2023). https://doi.org/10.1063/5.0155645

Rudy, W., Teodorczyk, A.: Numerical simulations of DDT limits in Hydrogen-Air Mixtures in obstacle laden channel. Energies (Basel) **14**, (2020). https://doi.org/10.3390/en14010024

Sitaraman, H., Yellapantula, S., Henry de Frahan, M.T., Perry, B., Rood, J., Grout, R., Day, M.: Adaptive mesh based combustion simulations of direct fuel injection effects in a supersonic cavity flame-holder. Combust. Flame **232**, 111531 (2021). https://doi.org/10.1016/j.combustflame.2021.111531

USCD: The San Diego mechanism - chemical-kinetic mechanisms for combustion applications. https://web.eng.ucsd.edu/mae/groups/combustion/mechanism.html (2023)

Valiev, D., Bychkov, V., Akkerman, V., Law, C.K., Eriksson, L.-E.: Flame acceleration in channels with obstacles in the deflagration-to-detonation transition. Combust. Flame **157**, 1012–1021 (2010). https://doi.org/10.1016/j.combustflame.2009.12.021

Xiao, H., Li, X.: Experimental and numerical study of flame acceleration and DDT in a channel with continuous obstacles. Combust. Theor. Model. **27**, 459–486 (2023). https://doi.org/10.1080/13647830.2023.2171905

Xiao, H., Oran, E.S.: Shock focusing and detonation initiation at a flame front. Combust. Flame **203**, 397–406 (2019). https://doi.org/10.1016/j.combustflame.2019.02.012

Zheng, K., Jia, Q., Ma, Z., Xing, Z., Hao, Y., Yu, M.: Experimental and numerical investigation on the premixed methane/air flame propagation in duct with obstacle gradients. Process Saf. Environ. Prot. **178**, 893–904 (2023). https://doi.org/10.1016/j.psep.2023.08.077

Zhou, Y., Williams, R.J.R., Ramaprabhu, P., Groom, M., Thornber, B., Hillier, A., Mostert, W., Rollin, B., Balachandar, S., Powell, P.D., Mahalov, A., Attal, N.: Rayleigh-taylor and Richtmyer-Meshkov instabilities: a journey through scales. Physica D **423**, 132838 (2021). https://doi.org/10.1016/j.physd.2020.132838

Authors and Affiliations

Sebastian Valencia[1] · Fernando Illacanchi[1] · Lucas de Azevedo[2,3] · Andres Z. Mendiburu[2,3] · Luis Bravo[4] · Prashant Khare[5,6] · Cesar Celis[1]

✉ Sebastian Valencia
svalenciar@pucp.edu.pe

[1] Mechanical Engineering Section, Pontificia Universidad Católica del Perú, Lima 15088, Peru

[2] Department of Mechanical Engineering, Federal University of Rio Grande do Sul, Porto Alegre, RS 90040-060, Brazil

[3] Detonations and Explosions Laboratory (LDE) – UFRGS, Porto Alegre, RS 90040-060, Brazil

[4] DEVCOM Army Research Laboratory, Army Research Directorate, Aberdeen Proving Ground, MD 21005, USA

[5] Department of Aerospace Engineering, University of Cincinnati, Cincinnati, OH 45221-0070, USA

[6] Hypersonics Laboratory, Digital Futures, University of Cincinnati, Cincinnati, OH 45221-0070, USA